

Simultaneous mapping of the ultrafast time and fluence dependence of the laser-induced insulator-to-metal transition in magnetite

J. O. Schunck^{1,2}, P. S. Miedema¹, R. Y. Engel^{1,2}, S. Dziarzhyski¹, G. Brenner¹, N. Ekanayake¹, C.-F. Chang⁴, P. Bougiatioti⁵, F. Döring⁵, B. Rösner⁵, C. David⁵, C. Schüßler-Langeheine⁶ and M. Beye^{1,2,3,*}

¹ Deutsches Elektronen-Synchrotron DESY, Notkestr. 85, 22607 Hamburg, Germany

² Physics Department, Universität Hamburg, Luruper Chaussee 149, 22761 Hamburg, Germany

³ Department of Physics, AlbaNova University Center, Stockholm University, SE-10691 Stockholm, Sweden

⁴ Max Planck Institute for Chemical Physics of Solids, Nöthnitzer Straße 40, 01187 Dresden, Germany.

⁵ Paul Scherrer Institut (PSI), Forschungsstraße 111, 5232 Villigen, Switzerland

⁶ Helmholtz-Zentrum Berlin für Materialien und Energie, Albert-Einstein-Straße 15, 12489 Berlin, Germany

* martin.beye@fysik.su.se

Abstract

Pump-probe methods are a ubiquitous tool in the field of ultrafast dynamic measurements. In recent years, X-ray free-electron laser experiments have gained importance due to their ability to probe with high chemical selectivity and at atomic length scales. To obtain the complete dynamic information, measurements are typically repeated many thousands of times with varying delay and/or fluence settings. This generally necessitates that the sample fully recovers before the subsequent excitation and that probe pulses and the induced dynamic evolution are comparable to each other. These conditions present a significant challenge when the sample fluctuates between different initial states or when it is susceptible to damage. Also, source fluctuations are normally intrinsic to free-electron laser pulses. Here, we present a time-to-space mapping imaging scheme that enables us to record a delay range of several picoseconds as well as a laser fluence range of about one order of magnitude in every single shot of the x-ray probe. This approach can circumvent the aforementioned preconditions. We demonstrate the use of this scheme by mapping the femto- and picosecond dynamics of the optically induced insulator-to-metal Verwey transition in a magnetite thin film. We employ resonant diffraction at the free-electron laser FLASH for probing. The dynamics of the magnetite thin film are found to follow a biexponential decay in line with earlier studies on bulk crystals. By extrapolating our results towards the conditions found at X-ray free-electron lasers with higher energy, we demonstrate that the presented data could be recorded in a single shot.

1 Introduction

The intriguing properties of complex, functional and quantum materials, like high-temperature superconductivity (1, 2), colossal magnetoresistance (3, 4), strange metallic behavior (5, 6), and insulator-metal phase transitions (7) have attracted researchers' interest on their quest to engineer and harvest these phenomena for several decades. Excitation with ultrashort laser pulses is a particularly powerful tool to manipulate equilibrium phases or create transient states which do not occur under equilibrium conditions (8–11). Usually, time-resolved studies are performed using two ultrashort pulses: the first pulse (the pump) starts a dynamic process, and the subsequent pulse (the probe) is used to observe the change induced in the sample. This pump-probe process is repeated thousands or millions of times while varying the temporal separation between the two pulses (the delay) and/or the fluence of the pump pulse.

X-ray free-electron lasers (FELs) offer the opportunity to use X-ray pulses for element-selective and atomic-scale probing with high signal levels and femtosecond temporal resolutions. Many FELs today generate pulses using the process of self-amplified spontaneous emission (SASE) (12–14), which results in fluctuating pulse properties, like intensity, pulse duration and spectral content. This characteristic motivated the development of techniques for recording a complete set of information for every single shot. In the post-analysis, the data can then be sorted and binned appropriately. In addition, such an approach also helps to detect non-reproducibility in the sample response itself, caused, e.g., by samples that fluctuate between different initial states (15, 16). Here, simultaneous detection of a range of parameters offers the opportunity to assign recorded data to its respective state, thereby facilitating a study of such systems in the first place. In repeated pump-probe experiments in general, one needs to take care that the sample is given enough time to return to the ground state and that the pulse energies are not too high to cause permanent damage to the sample. Alternatively, if the sample is destroyed by every shot, a new sample or spot on the sample needs to be used for every measurement (17), posing requirements on the available amount or size of sample. Many of these challenges can be alleviated using approaches that can do a complete experiment, i.e., measure the required delay (and potentially fluence) dependence in a single shot. One example of this approach is the X-ray streaking method (18–20), used at X-ray free-electron lasers to probe a delay range of approximately 1.5 ps in a single measurement.

Here, we present the results of setup that enables the simultaneous recording of a delay range of several picoseconds and a fluence range of about one order of magnitude. We use an X-ray optical Fresnel zone plate to image the iron L_3 -edge resonant soft X-ray diffraction (RSXD) signal from a magnetite sample. A non-collinear pump-probe geometry with an angle of approximately 70° between the pump and probe beams allows the pump-probe delay to be mapped onto a spatial axis on the detector (see Figure 1). The orthogonal axis images the signal across the laser beam spot onto the detector, essentially mapping the pump laser fluence distribution. With this setup, a large parameter range can be acquired in a static geometry without scanning. Given a sufficiently high signal, such a setup even allows capturing a complete dataset in a single shot.

As a sample, we chose a thin magnetite (Fe_3O_4) film. Being the first material in which a temperature-driven insulator-metal transition was discovered (21–24), magnetite continues to serve as a model system for how charge, orbital and lattice degrees of freedom shape the Verwey insulator-metal transition (25–34): Below the transition temperature of 124 K, the resistivity increases by two orders of magnitude due to an order-to-disorder transition (22). The high-temperature metallic phase has a cubic inverse-spinel crystal structure in which Fe^{3+} -ions occupy the tetrahedral (A) sites, whereas octahedral (B) sites are occupied by both Fe^{2+} and Fe^{3+} ions (26). When magnetite transitions to the low-temperature phase, the crystal unit cell doubles to a distorted monoclinic structure (35), characterized by charge and orbital order (COO) (23, 27–30) within the B-site Fe network. Emerging superstructure reflections can be accessed with RSXD e.g. at the iron $L_{2,3}$ -edges using the $(00\frac{1}{2})$ peak (the notation refers to the high-temperature unit cell) to probe the low-temperature order (29–32, 36). Accordingly, the reflections vanish in the high-temperature structure.

In the parallel detection setup, both the FEL and the probe laser illuminate an extended area on the order of one square millimeter on the sample, thus a homogeneous sample with flat high-quality surface is required. Here, a high-quality magnetite thin film was used. Besides being flat, thin films epitaxially grown on spinel Co_2TiO_4 substrates that closely match the crystal structure and lattice constant of magnetite have been shown to have excellent properties (37): In contrast to widely used magnesium oxide (MgO) substrates (38–40), the resistance hysteresis width of the Verwey transition matches that of the bulk, the correlation length of the COO is much larger than for films grown on MgO and comparable to bulk single

crystals, and the Verwey transition temperature even surpasses that of the bulk by 3 K.

As earlier experiments have shown, the excitation of the magnetite low-temperature phase with ultrashort infrared (IR) laser pulses destroys the COO superstructure and drives the system into the high-temperature structure within several picoseconds (41–46). Previous time-resolved IR pump, RSXD probe studies (41, 42) on magnetite bulk single crystals observed a two-step process on femto- and picosecond time scales, characterized by an initial sub-picosecond reduction of the scattering intensity caused by direct excitation of charge transfer between charge ordered sites (25, 43). The character of the ensuing evolution on the picosecond time scale depends on the pump fluence (42): For fluences below a temperature-dependent threshold (e.g. approximately 1.3 mJ/cm² at 80 K), only a few holes in the charge order are induced. The deposited energy is not sufficient to overcome the threshold of the phase transition so that the long-range order recovers within picoseconds. At fluences above this threshold, a transient non-equilibrium situation occurs with coexistence of insulating and metallic regions. Within several picoseconds, the volume fraction of the metallic phase grows, and the system evolves towards a homogeneous high-temperature phase. In this work, we observe a behavior of the thin film that is consistent with these findings, while acquiring the time- and fluence dependence simultaneously with every shot.

2 Experimental setup

Measurements with the time-to-space mapping setup were performed at beamline BL2 (47–49) of the free-electron laser (FEL) FLASH at DESY in Hamburg, Germany using the ultrahigh-vacuum diffractometer MUSIX (50). The schematic experimental setup is shown in Figure 1. To record resonant diffraction from a magnetite sample at the iron L_3 -edge at FLASH, third harmonic radiation with a central photon energy of 706 eV was used. The full width at half-maximum (FWHM) bandwidth of the FEL pulses was approximately 3.6 eV. The pulse energy of the FEL fundamental was on average 20 μ J and the third harmonic emission is usually two to three orders of magnitude weaker (51–53).

The unfocused FEL beam had a diameter of approximately 4.2 mm at the sample position. The pump laser (54) wavelength was centered around 800 nm, the pulse duration was 57 fs FWHM and the pulse energy was 16.8 μ J. The combined temporal

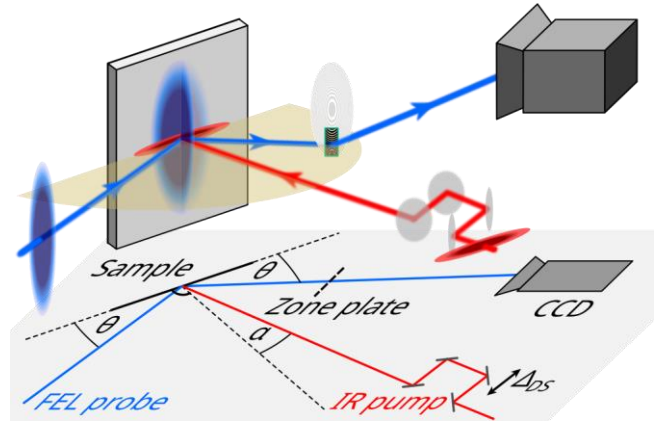


Figure 1: Time-to-space mapping setup. Soft X-ray pulses from FLASH resonant to the Fe L_3 edge (blue) probe the resonant scattering of Fe₃O₄ upon pumping with 800 nm pulses (red). The horizontal scattering plane is shown in yellow. The incidence and scattering angle θ is 32.75° with respect to the sample surface and the pump laser is incident onto the sample under an angle α of 16° with respect to the sample surface normal. Due to the relative angle between FEL and pump, a delay range of several picoseconds is probed simultaneously. An additional delay Δ_{DS} can be set by a mechanical delay stage. An off-axis Fresnel zone plate images the resonant scattering of the unfocused FEL beam from the sample onto a two-dimensional CCD detector.

resolution of the experiment was \sim 120 fs (see supplementary material). The laser spot measured approximately 2.6 mm (horizontal, FWHM) by 0.2 mm (vertical, FWHM) and was focused such that a flat-top region formed in the horizontal direction (see supplementary material, Figure S1). The sample was horizontally smaller than the laser footprint, extending only in the flat-top region of the laser focus. The pulse repetition rate of the FEL was 10 Hz, while that of the pump laser was 5 Hz so every other FEL shot probed the unpumped sample, serving as a reference for normalization of the signal. We verified that the sample was fully recovered in between shots. Due to the small third harmonic fraction of the FEL beam, the scattering cross-section of the sample and the large FEL footprint, the count rate for the data set was on average 0.54 counts/shot. In total, the data shown here comprises 12 h of acquisition time and approximately 230,000 counts.

The pump laser beam was incident under an angle of 16° with respect to the sample surface normal (see Figure 1). The sample was a 40 nm thin magnetite (Fe₃O₄) film, grown on Cr₂TiO₄(001) (37), measuring approximately 1.9 mm (horizontal) by 8 mm (vertical). The incidence angle θ of the FEL was 32.75° with

respect to the sample surface to fulfill the Bragg condition for the $(00\frac{1}{2})$ superstructure peak. The sample was cooled to a base temperature of 100 K for the entire duration of the measurements. An off-axis Fresnel zone plate (FZP) imaged the diffraction signal onto a two-dimensional charge-coupled device (CCD), thereby magnifying the diffraction signal from the sample by a factor of 4.1. Further details on the experimental setup can be found in the supplementary material.

The non-colinear geometry of FEL and pump laser was used as a time-to-space mapping setup (see Figure 1): Due to the angle between the two beams, the relative pulse front arrival time of both pulses varied along the horizontal dimension, thereby mapping a time (i.e. relative delay) axis to the horizontal space coordinate of the sample. With the FZP, the resonant diffraction signal from the sample, including this delay axis, was spatially resolved by imaging onto the detector. The delay range which can be covered in a single shot was determined by the geometry of the experiment (incident angles of FEL and laser beams), as well as the magnification of the FZP and the properties of the detector. In the present setup, the delay axis was mapped on the CCD as 23.6 fs/pixel. In principle, this would allow us to record a delay range of up to 50 ps, but in our experiment, the simultaneously recorded delay range was limited by the horizontal sample size to approximately 7 ps. Like in a conventional pump-probe scheme, the recorded delay range can be further extended by scanning the pump laser delay stage (Δ_{DS} in Figure 1).

In order to keep the laser profile rather homogeneous along the probed horizontal direction, which is used as delay axis, we used a cylindrical lens to focus the optical laser to a horizontal line on the sample. In the vertical direction, the laser is focused much stronger, well below the size of the probing FEL beam, such that the full vertical spatial laser profile was probed simultaneously. In the data analysis, we could thus separate regions in the center of the vertical laser spot profile, which were pumped with a high local fluence, from more weakly pumped regions further away.

Our imaging setup recorded two spatial dimensions simultaneously. We used our special experimental configuration to map the spatial coordinates onto one temporal and one local fluence axis. As this scheme introduces a correlation of signals recorded with different delays and fluences with sample position, it works best with samples that are spatially homogeneous over the probed area. But the scheme is also able to detect spatial inhomogeneities in the dynamical response: to this end, we scanned the

relative pump-probe delay Δ_{DS} (see Figure 1) back and forth by 3 ps using a movable delay stage, thereby moving the entire 7 ps delay window horizontally over the sample surface. This scan also served as a cross-calibration of the delay axis (see below and Figure 2). Scanning the pump laser spot in the vertical direction is not that simple but generally possible; also, the overall laser intensity could be varied. But even for a static laser spot, the correlation between fluence and vertical sample position can be checked, since the highest fluence occurs in an enlarged region around the center of the beam, while all other fluence regions appear twice in our data on both sides of the most intense part that can be compared. The detection of inhomogeneities in the dynamic response can occur within the spatial resolution of the setup, which we estimate to be around 3 μm to 4 μm for the present magnification (55).

3 Results

As described above, we obtained data as a function of the horizontal sample position, x , the vertical sample position, y , and the delay stage position, Δ_{DS} . How we obtain the calibration of the delay axis on the detector coordinates from this multidimensional data set, as well as data treatment steps used to obtain fluence-dependent delay traces, are visualized in Figure 2. Small regions of the sample imaged at delay stage positions Δ_{DS} of 0 ± 0.5 ps and 2 ± 0.5 ps are shown in panels (a) and (b), respectively. In both panels, the depicted pump signal has been normalized to the unpumped signal. The part of the sample where the COO was pumped away by the laser is visible as blue area. The horizontal position where both pulses cross the surface at the same time (time overlap, t_0) can be seen to be the x position where the signal transitions from high to low scattering intensity (black dashed lines). We chose the origin of the Δ_{DS} scale such that t_0 is in the horizontal center of the detector window ($x = 150$ px), see Figure 2(a).

The vertical profile of the signal which is averaged in the pumped area of panel (b) along the x -axis is shown as turquoise data in panel (c) of Figure 2. This profile maps the local strength of the pump-probe effect and follows the local fluence profile of the laser, which we show overlaid to the pump laser profile as extracted from an independent knife edge scan (green).

We now focus on calibrating the delay scale. For this, we use the region with the largest pump effect in the vertical center of the laser spot profile. We average the x -traces with pump fluences higher than 4 mJ/cm^2 and

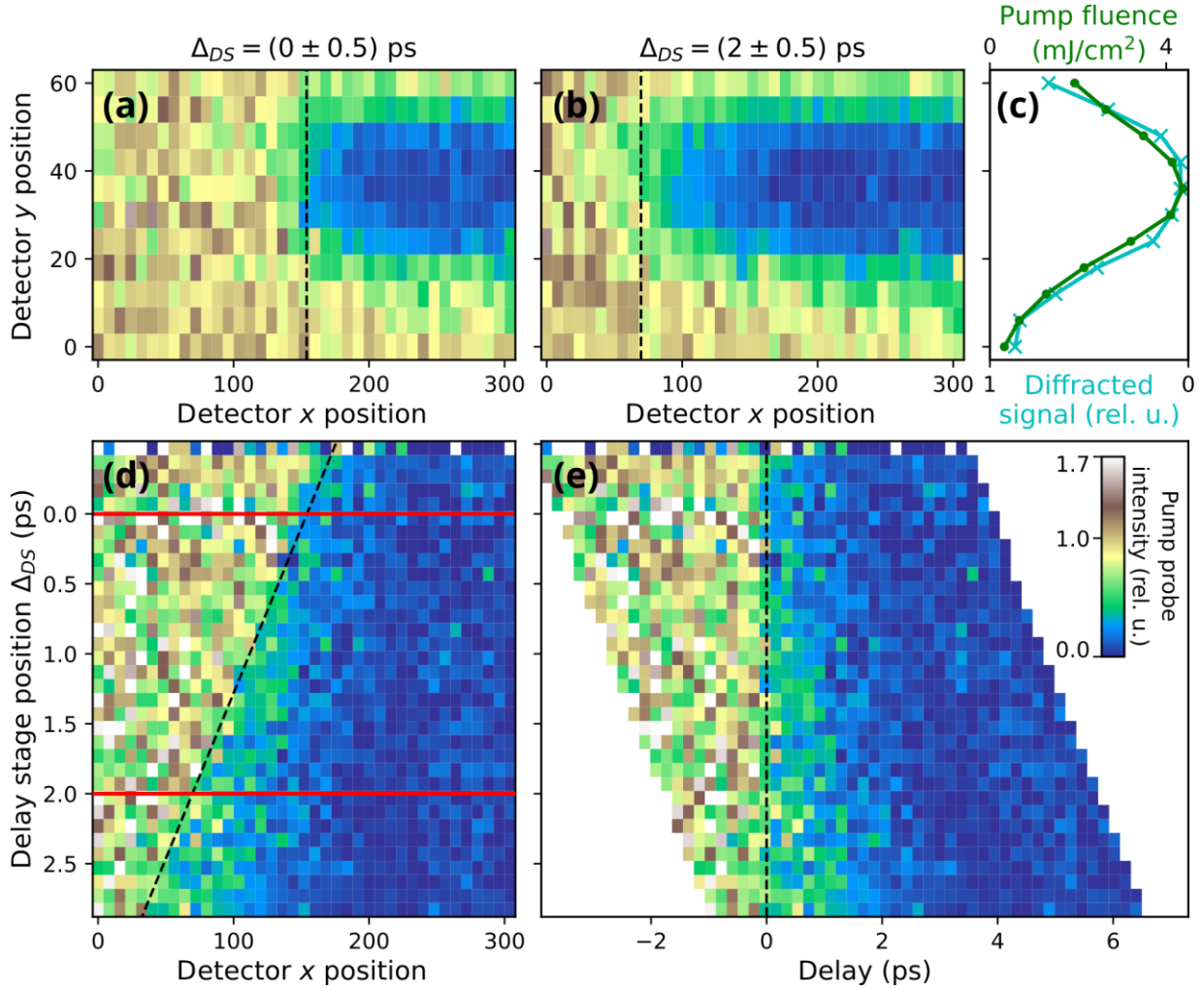


Figure 2: **Pump-probe data treatment.** The pump-probe delay varies along the horizontal x -axis because of the different incidence angles of FEL and pump laser. Panels (a), (b): Normalized images of the pump effect on the sample obtained by dividing pumped by unpumped events for delay stage position ranges of $\Delta_{DS} = (0 \pm 0.5)$ ps and $\Delta_{DS} = (2 \pm 0.5)$ ps, respectively. One positional unit on the detector corresponds to $13.5 \mu\text{m}$. Panel (c) shows the laser beam profile (green, upper axis) and the corresponding profile of the diffracted signal (cyan, lower axis), obtained by averaging only the pumped signal in panel (b) along the horizontal axis. Panel (d): By scanning the pump laser delay stage position Δ_{DS} (see also Figure 1) and plotting the average of detector y positions pumped with the highest fluences against the delay stage position (data shown along the red lines are extracted from panels (a) and (b)) allows one to observe how temporal overlap moves along x (black dashed line). The slope of the black dashed line can be used to translate every row onto a common delay axis. The x -axis and y -axis have been binned by a factor of 8 and 6, respectively. Panel (e) then shows the data set on the common horizontal delay axis, while the vertical axis still shows the mechanical delay stage position. Pump-probe traces as shown in Figure 3 are finally derived by averaging the data in panel (e) along the vertical dimension.

plot these for the different delay stage positions as a map (Figure 2(d)). t_0 extends along a diagonal (dashed line) reflecting the linear influences of both x and Δ_{DS} on the delay. The slope of this diagonal line yields the delay mapping factor on our detector (here 23.6 fs/px). This value depends on the relative incidence angle between FEL and pump laser, the sample and observation angles, the magnification of the imaging zone plate and the pixel size of the detector. By choosing these parameters, the setup-limited temporal resolution can be tuned to match the experimental requirements.

With this conversion, we can align each row to a common delay axis, see Figure 2(e). A common delay trace using all available data is then obtained by averaging the data in Figure 2(e) along the y axis. We note that there is a hint towards a small sample position dependence of the observed pump effect; it appears that the sample region that is mapped onto $x \approx 90$ exhibits a somewhat slower pump dynamics, which can be seen as a comparatively higher intensity around a delay value of 1 ps for delay stage positions of approximately 2.5 ps. However, the present data set does not have

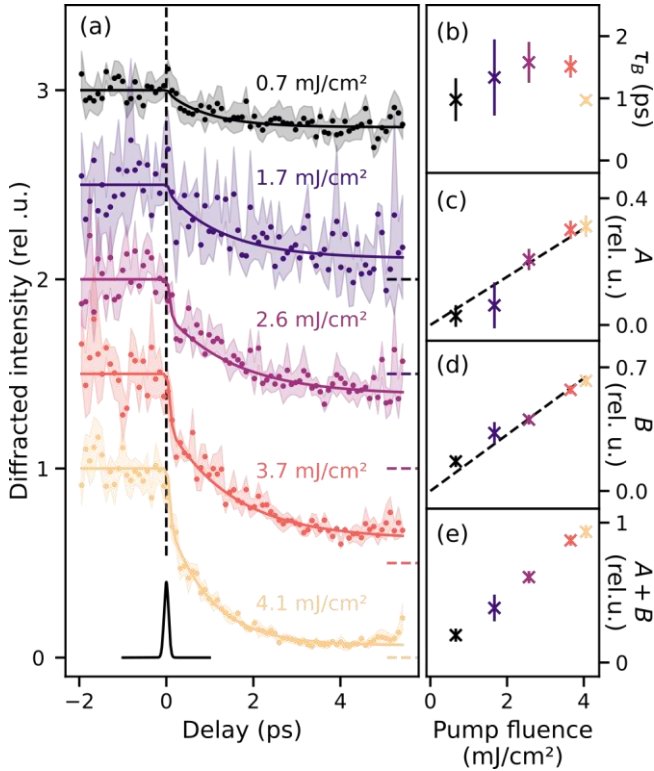


Figure 3: Ultrafast fluence-dependent response of a 40 nm thin magnetite film to 800 nm laser excitation. Panel (a): The intensity of the (00½) superstructure peak decreases on a few-picosecond time scale upon irradiation with the pump laser for fluences between 0.7 mJ/cm² and 4.1 mJ/cm². The data was normalized to 1 for negative delays and fit curves were offset by 0.5 relative units (rel. u.) for clarity, and the dashed lines to the right show 0 intensity for the data of the respective fluence. The shaded area is the one-sigma measurement uncertainty of the data, calculated as the standard deviation for each delay value upon averaging several traces of similar fluence and binning on the delay axis. Full lines show fits with a double exponential decay convolved with a Gaussian profile with a width corresponding to the experimental resolution, shown below in black at a delay of 0 ps. The fast time constant τ_A is set to be much faster than the temporal resolution. The fluence dependence of the slower time constant τ_B is shown in panel (b). Panels (c) and (d): Fluence dependence of the amplitudes A (fast process) and B (slow process) alongside linear trend lines with slopes $0.08 \text{ rel. u.}/(\text{mJ}/\text{cm}^2)$ and $0.16 \text{ rel. u.}/(\text{mJ}/\text{cm}^2)$, respectively. Panel (e): The total decay amplitude (i.e. sum of A and B). See supplementary material for details on the fitting procedure.

sufficient quality to study this rather weak effect in more detail.

Usually, the pump-fluence dependence of the ultrafast response of the sample to IR excitation is determined by repeating the pump-probe experiment with different pump laser attenuation settings. In our setup, we can do this by sorting different rows of the detector image according to the pump fluence at that position, see Figure 2(c). We chose to sort the data into five fluence bins (see supplementary material; Figure S2). Thus, we obtain five delay traces spanning a fluence range between 0.7 mJ/cm² and 4.1 mJ/cm² without actually changing the incident laser pulse energy. The resulting fluence-dependent IR pump, RSXD probe traces are depicted in Figure 3(a), showing a double exponential decay characterized by a fast and a slow component.

The resulting traces were fitted using a double exponential decay function (solid lines) convolved with a Gaussian of a width corresponding to the temporal resolution of the experiment (120 fs FWHM) as a fit model. The shaded regions in Fig. 3(a) show the experimental one-sigma standard deviation calculated for each data point during the averaging of multiple traces and binning on the x -axis. During the weighted least-squares fitting, the inverse experimental error is used as weights for the respective data points. We find that following the IR excitation, a fast and a slow decay process, respectively named A and B , occur, matching what has previously been observed for single crystals (41, 42, 56). Within our experimental uncertainty, there are no indications of a recovery in the measured delay range.

In panels (b) through (e) of Figure 3, the fluence dependence of the fit results for the slow decay time constant τ_B (b), the amplitudes A (c) and B (d) and the total long-time decrease $A+B$ (e) are shown. Error bars represent the one-sigma standard deviations. The fast decay is limited by the temporal resolution of the experiment to 120 fs. In the fitting procedure, this is realized by the convolution with the resolution-limited Gaussian function, therefore the value of τ_A was fixed to a value of 10 fs, much faster than the temporal resolution. Both amplitudes, A and B , show a linear increase with fluence of $0.08 \text{ rel. u.}/(\text{mJ}/\text{cm}^2)$ and $0.16 \text{ rel. u.}/(\text{mJ}/\text{cm}^2)$, respectively (black dashed lines in Figure 3(b) and (c)). The slow decay time constant τ_B ranges from 1 ps to 2 ps, generally matching previously reported values (42). See the supplementary material for more details on the fitting procedure.

4 Discussion

The IR pump, RSXD probe results obtained on magnetite thin films qualitatively match those

previously reported for single crystals (41, 42, 56): we find a biexponential decay with a fast time constant τ_A limited by the temporal resolution and a slow time constant on the picosecond scale. In the earlier studies, the fast process *A*, induced by the 800 nm pump, has been connected to electron transfer excitations from an Fe_B^{2+} to an Fe_B^{3+} ion (41–43, 46). This process directly alters the charge distribution and moves electrons between orbitals, which rapidly destroys charge and orbital order. We corroborate this within our resolution of 120 fs. The linear fluence dependence of amplitude *A*, previously reported for single crystals (42), is confirmed by our measurements. We find, however, quantitative differences beyond these generally agreeing results: (I) We do not observe two distinct fluence regimes with a ps recovery for low fluences and (II) the pump for the fast decay process seems to be less efficient than in earlier studies from bulk samples; the fluence dependence of the fast decay amplitude *A* has been reported to scale as 0.3 rel.u./(mJ/cm²) for single crystals, while we find 0.08 rel.u./(mJ/cm²) for the thin-films studied here. A saturation of this process is not apparent in our data, either. We discuss these differences in the following.

The two different fluence regimes (I) have been reported beyond a threshold fluence of approximately 1.3 mJ/cm² for an initial sample temperature of 80 K (42). The equivalent energy of this threshold corresponds to the heat, that would be necessary to drive the sample from its initial temperature through the Verwey transition temperature at 124 K under equilibrium conditions. Since we used a higher initial sample temperature of 100 K, the fluence threshold required to reach the high-fluence regime is expected to decrease according to the altered temperature difference between the base temperature and the Verwey transition temperature to approximately 0.7 mJ/cm² (41, 42, 57). While in principle we can extract data for very low fluence from the far wings of the vertical laser profile, the statistics of these data did not allow a quantitative analysis. The lowest fluence data that we could analyze corresponds to the expected threshold fluence, which explains the absence of recovery in the data set.

Concerning the different fluence dependencies of the amplitude *A* (II), we emphasize that a quantitative comparison of fluences in different experiments is challenging. Small deviations coming from differing calibrations in spot sizes and laser pulse energies, different estimates of sample reflectivity (that also relate to surface quality) as well as using different incidence angles and polarizations may add up to sizeable differences. For a quantitative comparison,

one would ideally study both sample types in the same setup. As intrinsic sample properties are concerned, differences between our magnetite thin film and a bulk magnetite crystal are expected to be small: A study directly comparing static RSXD and X-ray absorption data of thin films and bulk single crystals only finds minor spectral differences (36). In that study, MgO was used as a substrate for the thin film (as compared to Co₂TiO₄ for our study), which is arguably even less similar to bulk magnetite, judging by the very broad resistance hysteresis (37).

We can further rule out the limited film thickness as an explanation for this behavior, since the X-ray probing depth of around 10 nm to 40 nm (41, 42) is at most around the same as the film thickness. Therefore, even a much thicker bulk piece of magnetite is only probed at a depth corresponding roughly to the film thickness. Different thermal conductivities of the film substrate as compared to the bulk sample are expected to influence the evolution only on longer timescales than studied here.

Finally, the saturation of the fast process in single crystals has been observed at fluences above 2 mJ/cm², whereas we do not see saturation up to 4.1 mJ/cm². However, since the total decay amplitude is already very close to 1 at our highest fluence, we deduce from Figure 3(e) that we just missed the onset of saturation, which we expect to start at fluences around 4.3 mJ/cm² for our experiment.

In principle though, the nature of the thin film could support a different fluence dependence: In thin films, the presence of the Co₂TiO₄ substrate could influence the initial electron excitation by the IR pulse via strain which stabilizes the ordered low-temperature phase because Co₂TiO₄ has the same inverse spinel crystal structure as magnetite and only a small lattice mismatch of +0.66%, resulting in the increased transition temperature in these films as compared to the bulk (37). The mechanism behind this stabilization is thought to be tensile strain imposed by the substrate, resulting in increased lattice constants in the film plane. Enlarged inter-atomic distances facilitate the formation of the ordered state, hence an increased transition temperature is observed (37). As a consequence of this stabilization of the ordered phase, the electron transfer from Fe_B^{2+} to Fe_B^{3+} sites, which is the process of the initial destruction of the order, may be energetically more expensive. Per incident IR photon, fewer charge transfer excitations could take place leading to a shift of saturation to higher fluences. However, the observed differences in fluence at which saturation of process *A* occurs and the slope of amplitude *A* with fluence can likely not be entirely explained by the influence of the

substrate, as the Co_2TiO_4 substrate leads to a comparably minor increase in transition temperature from 124 K (bulk) to 127 K.

Therefore, we attribute most of the quantitative differences in the fluence dependence to differing experimental conditions and according uncertainties in cross-calibrating experimental variables. A potential stabilization of the ordered phase in the thin film, originating from the substrate, could enhance the observed difference, but typical reproducibility errors in such setups do not allow for a more rigorous conclusion.

5 Conclusion and Outlook

In this study, we present results of a time-to-space mapping setup for time-resolved pump-probe experiments. This setup is capable of recording an extended delay range (dependent on the dimensions of the sample and the laser and FEL beams) and a fluence range of approximately one order of magnitude in a static setup, without the need for any scans. This is achieved within a range of a few millimeters on the sample where the pump laser and FEL overlap, both incident under a relative angle of about 70° . Due to this angle, the relative delay of both pulses is imprinted into the horizontal dimension on the sample and imaged onto the detector with a Fresnel zone plate. In the vertical direction, imaging the laser spot profile allows for the simultaneous probing of regions of the sample that have been pumped by higher (in the center of the spot) or lower (at the edges of the spot) fluences.

With this setup, the ultrafast phase transition dynamics of high-quality magnetite (Fe_3O_4) thin films was investigated, induced by 800 nm laser pulses using resonant soft X-ray diffraction at the iron L_3 -edge as probe. The induced dynamics generally match those previously observed in single crystals: A biexponential decay of charge and orbital order constituted of a fast process (sub 120 fs) and a slower process (1 ps to 2 ps). The former has been assigned to charge transfer within the B-site Fe network, while the latter has been attributed to the reorganization of remaining charge-ordered islands within an otherwise metallic surrounding. The amplitudes of both decay processes are found to linearly depend on the fluence up to a value of 4.1 mJ/cm^2 . Although saturation is not observed at the highest fluence, we expect that saturation will occur around 4.3 mJ/cm^2 .

We ascribe the quantitatively different dynamic behavior of the fluence dependence in comparison to single crystals to mainly originate from different

experimental conditions with a potential minor contribution from the influence of the thin-film substrate.

Excitingly, our setup can be used to record full datasets on laser-induced dynamics in a single shot with complete information on time- and fluence dependences. Optimized experiments can achieve a dramatically increased signal level which exceeds the one in our demonstration by more than six orders of magnitude as we discuss in the following: The used pulses from FLASH had $20 \mu\text{J}$ pulse energy in the fundamental with an expected contribution at the Fe L -edge of about 20 nJ. Higher-energy FELs, like the European XFEL, PALFEL, SwissFEL or LCLS, can typically produce mJ level pulse energies at these photon energies (58), which yields an intensity gain of five orders of magnitude. Additionally, focusing the FEL beam to a line measuring $2 \times 0.2 \text{ mm}^2$ and therefore matching the studied area yields another gain of more than an order of magnitude compared to the round spot with about 4.2 mm diameter we used here. With these improvements, the signal level of a single shot has the potential to substantially surpass that of the full data set presented here. We show here results from 12 h acquisition with an average of about 0.5 counts/shot, equal to averaging about 230,000 shots from the FEL. These improvements can yield an increase in signal of more than six orders of magnitude, demonstrating that single shot acquisition of a complete dataset on ultrafast dynamics of sensitive samples including delay and fluence dependences is feasible.

We note though that the conditions described above result in probe fluences of about 500 mJ/cm^2 , which is certainly beyond the damage threshold of the majority of solids. Consequently, single-shot acquisition becomes a necessity in a measure-before-destroy approach. In order to reduce the probe fluence to a level of $<1 \text{ mJ/cm}^2$, which should be tolerable and non-disturbing to most samples (59), the FEL pulse could be attenuated by about one order of magnitude while still yielding a data set of comparable quality to that shown here. The remaining about two orders of magnitude can be recovered by increasing the probe spot size optimized to the studied delay and pump fluence ranges and tolerable probe fluence. Consequently, the spot size of the optical pump laser would need to be increased accordingly, necessitating an increase in pulse energy to adequately excite the sample.

6 Supplementary Material

The supplementary material provides some more detailed information on the calibration of the pump laser fluences, experimental parameters (temporal resolution of the setup, Fresnel zone plate optic and detector) and the fitting procedure of the pump-probe delay traces.

7 Acknowledgments

The setup as well as MB, PSM, RYE and JOS are funded through a grant to MB for a Helmholtz young investigator group under contract number VH-NG-1105. CSL acknowledges funding by the Deutsche Forschungsgemeinschaft (DFG, German Research Foundation)– Project-ID 328545488 – TRR 227. We acknowledge DESY (Hamburg, Germany), a member of the Helmholtz Association HGF, for the provision of experimental facilities. Parts of this research were carried out at FLASH and we would like to thank Sven Toleikis for helpful discussions and assistance in using beamline BL2, as well as the DESY machine and photon operators for assistance in using the FEL beam. Beamtime was allocated for proposals F-20170534 and F-20181193.

8 Author Declarations

Conflicts of interest

The authors have no conflicts to disclose.

10 References

1. J. G. Bednorz, K. A. Müller, Possible High Tc Superconductivity in the Ba-La-Cu-O System. *Zeitschrift für Phys. B Condens. Matter* **64**, 189–193 (1986).
2. B. Keimer, S. A. Kivelson, M. R. Norman, S. Uchida, J. Zaanen, From quantum matter to high-temperature superconductivity in copper oxides. *Nature* **518**, 179–186 (2015).
3. E. Dagotto, T. Hotta, A. Moreo, Colossal magnetoresistant materials: the key role of phase separation. *Phys. Rep.* **344**, 1–153 (2001).
4. E. Dagotto, Complexity in strongly correlated electronic systems. *Science*. **309**, 257–262 (2005).
5. H. Takagi, B. Batlogg, H. L. Kao, J. Kwo, R. J. Cava, J. J. Krajewski, W. F. Peck, Systematic evolution of temperature-dependent resistivity in $\text{La}_{2-x}\text{Sr}_x\text{CuO}_4$. *Phys. Rev. Lett.* **69**, 2975–2978 (1992).
6. P. W. Phillips, N. E. Hussey, P. Abbamonte, Stranger than metals. *Science* **377** (2022).
7. M. Imada, A. Fujimori, Y. Tokura, Metal-insulator transitions. *Rev. Mod. Phys.* **70**, 1039–1263 (1998).
8. J. Orenstein, Ultrafast spectroscopy of quantum materials. *Phys. Today* **65**, 44–50 (2012).

Author contributions

J.O.S. Formal Analysis (lead), Investigation (equal), Visualization (lead), Writing/Original Draft Preparation (equal), Writing/Review & Editing (lead). **P.S.M.** Investigation (equal), Writing/Review & Editing (equal). **R.Y.E.** Formal Analysis (supporting), Investigation (equal), Writing/Review & Editing (equal). **S.D.** Investigation (equal), Writing/Review & Editing (equal). **G.B.** Investigation (equal), Writing/Review & Editing (equal). **N.E.** Investigation (equal), Resources (equal), Writing/Review & Editing (equal). **C.-F.C.** Resources (equal), Writing/Review & Editing (equal). **P.B.** Investigation (equal), Writing/Review & Editing (equal). **F.D.** Resources (equal), Writing/Review & Editing (equal). **B.R.** Investigation (equal), Resources (equal), Writing/Review & Editing (equal). **C.D.** Resources (equal), Writing/Review & Editing (equal). **C.S-L.** Conceptualization (equal), Investigation (equal), Writing/Original Draft Preparation (equal), Writing/Review & Editing (equal). **M.B.** Conceptualization (lead), Funding Acquisition (lead), Investigation (equal), Project Administration (lead), Supervision (lead), Writing/Original Draft Preparation (equal), Writing/Review & Editing (equal).

9 Data Availability Statement

The data that supports the findings of this study are available from the corresponding author upon reasonable request.

9. M. Mitrano, Y. Wang, Probing light-driven quantum materials with ultrafast resonant inelastic X-ray scattering. *Commun. Phys.* **3**, 1–9 (2020).
10. A. de la Torre, D. M. Kennes, M. Claassen, S. Gerber, J. W. McIver, M. A. Sentef, Colloquium: Nonthermal pathways to ultrafast control in quantum materials. *Rev. Mod. Phys.* **93**, 041002 (2021).
11. A. Zong, B. R. Nebgen, S.-C. Lin, J. A. Spies, M. Zuerch, Emerging ultrafast techniques for studying quantum materials. *Nat. Rev. Mater.* **8**, 224–240 (2023).
12. A. M. Kondratenko, E. L. Saldin, Generation of Coherent Radiation by a Relativistic Electron Beam in an Undulator. *Part. Accel.* **10**, 207–216 (1980).
13. S. V. Milton, E. Gluskin, N. D. Arnold, C. Benson, W. Berg, S. G. Biedron, M. Borland, Y.-C. Chae, R. J. Dejus, P. K. Den Hartog, B. Deriy, M. Erdmann, Y. I. Eidelman, M. W. Hahne, Z. Huang, K.-J. Kim, J. W. Lewellen, Y. Li, A. H. Lumpkin, O. Makarov, E. R. Moog, A. Nassiri, V. Sajaev, R. Soliday, B. J. Tieman, E. M. Trakhtenberg, G. Travish, I. B. Vasserman, N. A. Vinokurov, X. J. Wang, G. Wiemerslage, B. X. Yang, Exponential Gain and Saturation of a Self-Amplified Spontaneous Emission Free-Electron Laser. *Science* **292**, 2037–2041 (2001).
14. J. Rönsch-Schulenburg, E. Hass, N. M. Lockmann, T. Plath, M. Rehders, J. Roßbach, G. Brenner, S. Dziarzhytski, T. Golz, H. Schlarb, B. Schmidt, E. Schneidmiller, S. Schreiber, B. Steffen, N. Stojanovic, S. Wunderlich, M. Yurkov, Operation of FLASH with short SASE-FEL radiation pulses. *Proc. 36th Int. Free Electron Laser Conf. FEL 2014*, 342–345 (2014).
15. T. Wang, D. Zhu, B. Wu, C. Graves, S. Schaffert, T. Rander, L. Müller, B. Vodungbo, C. Baumier, D. P. Bernstein, B. Bräuer, V. Cros, S. de Jong, R. Delaunay, A. Fognini, R. Kukreja, S. Lee, V. López-Flores, J. Mohanty, B. Pfau, H. Popescu, M. Sacchi, A. B. Sardinha, F. Sirotti, P. Zeitoun, M. Messerschmidt, J. J. Turner, W. F. Schlotter, O. Hellwig, R. Mattana, N. Jaouen, F. Fortuna, Y. Acremann, C. Gutt, H. A. Dürr, E. Beaupaire, C. Boeglin, S. Eisebitt, G. Grübel, J. Lüning, J. Stöhr, A. O. Scherz, Femtosecond Single-Shot Imaging of Nanoscale Ferromagnetic Order in CoPd Multilayers Using Resonant X-Ray Holography. *Phys. Rev. Lett.* **108**, 267403 (2012).
16. C. Klose, F. Büttner, W. Hu, C. Mazzoli, K. Litzius, R. Battistelli, S. Zayko, I. Lemesh, J. M. Bartell, M. Huang, C. M. Günther, M. Schneider, A. Barbour, S. B. Wilkins, G. S. D. Beach, S. Eisebitt, B. Pfau, Coherent correlation imaging for resolving fluctuating states of matter. *Nature* **614**, 256–261 (2023).
17. S. M. Vinko, O. Ciricosta, B. I. Cho, K. Engelhorn, H.-K. Chung, C. R. D. Brown, T. Burian, J. Chalupský, R. W. Falcone, C. Graves, V. Hájková, A. Higginbotham, L. Juha, J. Krzywinski, H. J. Lee, M. Messerschmidt, C. D. Murphy, Y. Ping, A. Scherz, W. Schlotter, S. Toleikis, J. J. Turner, L. Vysin, T. Wang, B. Wu, U. Zastrau, D. Zhu, R. W. Lee, P. A. Heimann, B. Nagler, J. S. Wark, Creation and diagnosis of a solid-density plasma with an X-ray free-electron laser. *Nature* **482**, 59–62 (2012).
18. C. David, P. Karvinen, M. Sikorski, S. Song, I. Vartiainen, C. J. Milne, A. Mozzanica, Y. Kayser, A. Diaz, I. Mohacsi, G. A. Carini, S. Herrmann, E. Färm, M. Ritala, D. M. Fritz, A. Robert, Following the dynamics of matter with femtosecond precision using the X-ray streaking method. *Sci. Rep.* **5**, 7644 (2015).
19. M. Buzzi, M. Makita, L. Howald, A. Kleibert, B. Vodungbo, P. Maldonado, J. Raabe, N. Jaouen, H. Redlin, K. Tiedtke, P. M. Oppeneer, C. David, F. Nolting, J. Lüning, Single-shot Monitoring of Ultrafast Processes via X-ray Streaking at a Free Electron Laser. *Sci. Rep.* **7**, 7253 (2017).
20. E. Jal, M. Makita, B. Rösner, C. David, F. Nolting, J. Raabe, T. Savchenko, A. Kleibert, F. Capotondi, E. Pedersoli, L. Raimondi, M. Manfredda, I. Nikolov, X. Liu, A. E. D. Merhe, N. Jaouen, J. Gorchon, G. Malinowski, M. Hehn, B. Vodungbo, J. Lüning, Single-shot time-resolved magnetic x-ray absorption at a free-electron laser. *Phys. Rev. B* **99**, 144305 (2019).
21. E. J. W. Verwey, Electronic Conduction of Magnetite (Fe₃O₄) and its Transition Point at Low Temperatures. *Nature* **144**, 327 (1939).
22. E. J. W. Verwey, P. W. Haayman, Electronic conductivity and transition point of magnetite (“Fe₃O₄”). *Physica* **8**, 979–987 (1941).
23. F. Walz, The Verwey transition - A topical review. *J. Phys. Condens. Matter* **14**, 285–340 (2002).
24. J. García, G. Subías, The Verwey transition—a new perspective. *J. Phys. Condens. Matter* **16**, R145–R178

(2004).

25. S. K. Park, T. Ishikawa, Y. Tokura, Charge-gap formation upon the Verwey transition in Fe_3O_4 . *Phys. Rev. B* **58**, 3717–3720 (1998).
26. J. P. Wright, J. P. Attfield, P. G. Radaelli, Long Range Charge Ordering in Magnetite Below the Verwey Transition. *Phys. Rev. Lett.* **87**, 266401 (2001).
27. J. P. Wright, J. P. Attfield, P. G. Radaelli, Charge ordered structure of magnetite Fe_3O_4 below the Verwey transition. *Phys. Rev. B* **66**, 214422 (2002).
28. I. Leonov, A. N. Yaresko, V. N. Antonov, M. A. Korotin, V. I. Anisimov, Charge and Orbital Order in Fe_3O_4 . *Phys. Rev. Lett.* **93**, 146404 (2004).
29. D. J. Huang, H.-J. Lin, J. Okamoto, K. S. Chao, H.-T. Jeng, G. Y. Guo, C.-H. Hsu, C.-M. Huang, D. C. Ling, W. B. Wu, C. S. Yang, C. T. Chen, Charge-Orbital Ordering and Verwey Transition in Magnetite Measured by Resonant Soft X-Ray Scattering. *Phys. Rev. Lett.* **96**, 096401 (2006).
30. J. Schlappa, C. Schüßler-Langeheine, C. F. Chang, H. Ott, A. Tanaka, Z. Hu, M. W. Haverkort, E. Schierle, E. Weschke, G. Kaindl, L. H. Tjeng, Direct Observation of t_{2g} Orbital Ordering in Magnetite. *Phys. Rev. Lett.* **100**, 026406 (2008).
31. A. Tanaka, C. F. Chang, M. Buchholz, C. Trabant, E. Schierle, J. Schlappa, D. Schmitz, H. Ott, P. Metcalf, L. H. Tjeng, C. Schüßler-Langeheine, Symmetry of Orbital Order in Fe_3O_4 Studied by Fe $L_{2,3}$ Resonant X-Ray Diffraction. *Phys. Rev. Lett.* **108**, 227203 (2012).
32. A. Tanaka, C. F. Chang, M. Buchholz, C. Trabant, E. Schierle, J. Schlappa, D. Schmitz, H. Ott, P. Metcalf, L. H. Tjeng, C. Schüßler-Langeheine, Analysis of charge and orbital order in Fe_3O_4 by Fe $L_{2,3}$ resonant x-ray diffraction. *Phys. Rev. B* **88**, 195110 (2013).
33. M. Hoesch, P. Piekarczyk, A. Bosak, M. Le Tacon, M. Krisch, A. Kozłowski, A. M. Oleś, K. Parlinski, Anharmonicity due to Electron-Phonon Coupling in Magnetite. *Phys. Rev. Lett.* **110**, 207204 (2013).
34. A. Bosak, D. Chernyshov, M. Hoesch, P. Piekarczyk, M. Le Tacon, M. Krisch, A. Kozłowski, A. M. Oleś, K. Parlinski, Short-Range Correlations in Magnetite above the Verwey Temperature. *Phys. Rev. X* **4**, 011040 (2014).
35. M. S. Senn, J. P. Wright, J. P. Attfield, Charge order and three-site distortions in the Verwey structure of magnetite. *Nature* **481**, 173–176 (2012).
36. C. F. Chang, J. Schlappa, M. Buchholz, A. Tanaka, E. Schierle, D. Schmitz, H. Ott, R. Sutarto, T. Willers, P. Metcalf, L. H. Tjeng, C. Schüßler-Langeheine, Intrinsic and extrinsic x-ray absorption effects in soft x-ray diffraction from the superstructure in magnetite. *Phys. Rev. B* **83**, 073105 (2011).
37. X. Liu, C.-F. Chang, A. D. Rata, A. C. Komarek, L. H. Tjeng, Fe_3O_4 thin films: controlling and manipulating an elusive quantum material. *npj Quantum Mater.* **1**, 16027 (2016).
38. W. Eerenstein, T. T. M. Palstra, T. Hibma, S. Celotto, Origin of the increased resistivity in epitaxial Fe_3O_4 films. *Phys. Rev. B* **66**, 201101 (2002).
39. S. K. Arora, R. G. S. Sofin, I. V. Shvets, Magnetoresistance enhancement in epitaxial magnetite films grown on vicinal substrates. *Phys. Rev. B* **72**, 134404 (2005).
40. X. H. Liu, A. D. Rata, C. F. Chang, A. C. Komarek, L. H. Tjeng, Verwey transition in Fe_3O_4 thin films: Influence of oxygen stoichiometry and substrate-induced microstructure. *Phys. Rev. B* **90**, 125142 (2014).
41. N. Pontius, T. Kachel, C. Schüßler-Langeheine, W. F. Schlotter, M. Beye, F. Sorgenfrei, C. F. Chang, A. Föhlisch, W. Wurth, P. Metcalf, I. Leonov, A. Yaresko, N. Stojanovic, M. Berglund, N. Guerassimova, S. Düsterer, H. Redlin, H. A. Dürr, Time-resolved resonant soft x-ray diffraction with free-electron lasers: Femtosecond dynamics across the Verwey transition in magnetite. *Appl. Phys. Lett.* **98**, 182504 (2011).
42. S. de Jong, R. Kukreja, C. Trabant, N. Pontius, C. F. Chang, T. Kachel, M. Beye, F. Sorgenfrei, C. H. Back, B. Bräuer, W. F. Schlotter, J. J. Turner, O. Krupin, M. Doehler, D. Zhu, M. A. Hossain, A. O. Scherz, D. Fausti, F. Novelli, M. Esposito, W. S. Lee, Y. D. Chuang, D. H. Lu, R. G. Moore, M. Yi, M. Trigo, P. Kirchmann, L. Pathey, M. S. Golden, M. Buchholz, P. Metcalf, F. Parmigiani, W. Wurth, A.

- Föhlisch, C. Schüßler-Langeheine, H. A. Dürr, Speed limit of the insulator–metal transition in magnetite. *Nat. Mater.* **12**, 882–886 (2013).
43. F. Randi, I. Vergara, F. Novelli, M. Esposito, M. Dell’Angela, V. A. M. Brabers, P. Metcalf, R. Kukreja, H. A. Dürr, D. Fausti, M. Grüninger, F. Parmigiani, Phase separation in the nonequilibrium Verwey transition in magnetite. *Phys. Rev. B* **93**, 054305 (2016).
 44. E. Baldini, C. A. Belvin, M. Rodriguez-Vega, I. O. Ozel, D. Legut, A. Kozłowski, A. M. Oleś, K. Parlinski, P. Piekarczyk, J. Lorenzana, G. A. Fiete, N. Gedik, Discovery of the soft electronic modes of the trimeron order in magnetite. *Nat. Phys.* **16**, 541–545 (2020).
 45. W. Wang, J. Li, Z. Liang, L. Wu, P. M. Lozano, A. C. Komarek, X. Shen, A. H. Reid, X. Wang, Q. Li, W. Yin, K. Sun, I. K. Robinson, Y. Zhu, M. P. M. Dean, J. Tao, Verwey transition as evolution from electronic nematicity to trimerons via electron-phonon coupling. *Sci. Adv.* **9**, eadf8220 (2023).
 46. B. Truc, P. Usai, F. Pennacchio, G. Berruto, R. Claude, I. Madan, V. Sala, T. LaGrange, G. M. Vanacore, S. Benhabib, F. Carbone, Ultrafast generation of hidden phases via energy-tuned electronic photoexcitation in magnetite. *Proc. Natl. Acad. Sci.* **121**, e2316438121 (2024).
 47. K. Tiedtke, A. Azima, N. von Bargen, L. Bittner, S. Bonfigt, S. Düsterer, B. Faatz, U. Frühling, M. Gensch, C. Gerth, N. Guerassimova, U. Hahn, T. Hans, M. Hesse, K. Honkavaara, U. Jastrow, P. Juranic, S. Kapitzki, B. Keitel, T. Kracht, M. Kuhlmann, W. B. Li, M. Martins, T. Núñez, E. Plönjes, H. Redlin, E. L. Saldin, E. A. Schneidmiller, J. R. Schneider, S. Schreiber, N. Stojanovic, F. Tavella, S. Toleikis, R. Treusch, H. Weigelt, M. Wellhöfer, H. Wabnitz, M. V. Yurkov, J. Feldhaus, The soft x-ray free-electron laser FLASH at DESY: beamlines, diagnostics and end-stations. *New J. Phys.* **11**, 023029 (2009).
 48. J. Feldhaus, FLASH—the first soft x-ray free electron laser (FEL) user facility. *J. Phys. B At. Mol. Opt. Phys.* **43**, 194002 (2010).
 49. S. Toleikis, The FLASH facility current status in 2018 and future upgrade plans. *AIP Conf. Proc.* **2054**, 030015 (2019).
 50. M. Beye, R. Y. Engel, J. O. Schunck, S. Dziarzhytski, G. Brenner, P. S. Miedema, Non-linear soft x-ray methods on solids with MUSIX—the multi-dimensional spectroscopy and inelastic x-ray scattering endstation. *J. Phys. Condens. Matter* **31**, 014003 (2019).
 51. E. L. Saldin, E. A. Schneidmiller, M. V. Yurkov, Properties of the third harmonic of the radiation from self-amplified spontaneous emission free electron laser. *Phys. Rev. Spec. Top. - Accel. Beams* **9**, 030702 (2006).
 52. S. Düsterer, P. Radcliffe, G. Geloni, U. Jastrow, M. Kuhlmann, E. Plönjes, K. Tiedtke, R. Treusch, J. Feldhaus, P. Nicolosi, L. Poletto, P. Yeates, H. Luna, J. T. Costello, P. Orr, D. Cubaynes, M. Meyer, Spectroscopic characterization of vacuum ultraviolet free electron laser pulses. *Opt. Lett.* **31**, 1750 (2006).
 53. W. Ackermann, G. Asova, V. Ayvazyan, A. Azima, N. Baboi, J. Bähr, V. Balandin, B. Beutner, A. Brandt, A. Bolzmann, R. Brinkmann, O. I. Brovko, M. Castellano, P. Castro, L. Catani, E. Chiadroni, S. Choroba, A. Cianchi, J. T. Costello, D. Cubaynes, J. Dardis, W. Decking, H. Delsim-Hashemi, A. Delsérieys, G. Di Pirro, M. Dohlus, S. Düsterer, A. Eckhardt, H. T. Edwards, B. Faatz, J. Feldhaus, K. Flöttmann, J. Frisch, L. Fröhlich, T. Garvey, U. Gensch, C. Gerth, M. Görler, N. Golubeva, H.-J. Grabosch, M. Grecki, O. Grimm, K. Hacker, U. Hahn, J. H. Han, K. Honkavaara, T. Hott, M. Hüning, Y. Ivanisenko, E. Jaeschke, W. Jalmuzna, T. Jezynski, R. Kammering, V. Katalev, K. Kavanagh, E. T. Kennedy, S. Khodyachykh, K. Klose, V. Kocharyan, M. Körfer, M. Kollwe, W. Koprek, S. Korepanov, D. Kostin, M. Krassilnikov, G. Kube, M. Kuhlmann, C. L. S. Lewis, L. Lilje, T. Limberg, D. Lipka, F. Lühl, H. Luna, M. Luong, M. Martins, M. Meyer, P. Michelato, V. Miltchev, W. D. Möller, L. Monaco, W. F. O. Müller, O. Napieralski, O. Napoly, P. Nicolosi, D. Nölle, T. Nuñez, A. Oppelt, C. Pagani, R. Paparella, N. Pchalek, J. Pedregosa-Gutierrez, B. Petersen, B. Petrosyan, G. Petrosyan, L. Petrosyan, J. Pflüger, E. Plönjes, L. Poletto, K. Pozniak, E. Prat, D. Proch, P. Pucyk, P. Radcliffe, H. Redlin, K. Rehlich, M. Richter, M. Roehrs, J. Roensch, R. Romaniuk, M. Ross, J. Rossbach, V. Rybnikov, M. Sachwitz, E. L. Saldin, W. Sandner, H. Schlarb, B. Schmidt, M. Schmitz, P. Schmüser, J. R. Schneider, E. A. Schneidmiller, S. Schnepf, S. Schreiber, M. Seidel, D. Sertore, A. V. Shabunov, C. Simon, S. Simrock, E. Sombrowski, A. A. Sorokin, P. Spanknebel, R. Spesyvtsev, L. Staykov, B. Steffen, F. Stephan, F. Stulle, H. Thom, K. Tiedtke, M. Tischer, S. Toleikis, R. Treusch, D. Trines, I. Tsakov, E. Vogel, T. Weiland, H. Weise, M. Wellhöfer, M. Wendt, I. Will, A. Winter, K. Wittenburg, W. Wurth, P. Yeates, M. V. Yurkov, I. Zagorodnov, K. Zapfe,

Operation of a free-electron laser from the extreme ultraviolet to the water window. *Nat. Photonics* **1**, 336–342 (2007).

54. H. Redlin, A. Al-Shemmary, A. Azima, N. Stojanovic, F. Tavella, I. Will, S. Düsterer, The FLASH pump–probe laser system: Setup, characterization and optical beamlines. *Nucl. Instruments Methods Phys. Res. Sect. A Accel. Spectrometers, Detect. Assoc. Equip.* **635**, S88–S93 (2011).
55. J. O. Schunck, F. Döring, B. Rösner, J. Buck, R. Y. Engel, P. S. Miedema, S. K. Mahatha, M. Hoesch, A. Petraru, H. Kohlstedt, C. Schüßler-Langeheine, K. Rossnagel, C. David, M. Beye, Soft x-ray imaging spectroscopy with micrometer resolution. *Optica* **8**, 156 (2021).
56. N. Pontius, M. Beye, C. Trabant, R. Mitzner, F. Sorgenfrei, T. Kachel, M. Wöstmann, S. Roling, H. Zacharias, R. Ivanov, R. Treusch, M. Buchholz, P. Metcalf, C. Schüßler-Langeheine, A. Föhlisch, Probing the non-equilibrium transient state in magnetite by a jitter-free two-color X-ray pump and X-ray probe experiment. *Struct. Dyn.* **5**, 054501 (2018).
57. E. F. Westrum, F. Grønvold, Magnetite (Fe₃O₄) Heat capacity and thermodynamic properties from 5 to 350 K, low-temperature transition. *J. Chem. Thermodyn.* **1**, 543–557 (1969).
58. T. Tschentscher, C. Bressler, J. Grünert, A. Madsen, A. Mancuso, M. Meyer, A. Scherz, H. Sinn, U. Zastra, Photon Beam Transport and Scientific Instruments at the European XFEL. *Appl. Sci.* **7**, 592 (2017).
59. R. Y. Engel, O. Alexander, K. Atak, U. Bovensiepen, J. Buck, R. Carley, M. Cascella, V. Chardonnet, G. S. Chiuzaian, C. David, F. Döring, A. Eschenlohr, N. Gerasimova, F. de Groot, L. Le Guyader, O. S. Humphries, M. Izquierdo, E. Jal, A. Kubec, T. Laarmann, C.-H. Lambert, J. Lüning, J. P. Marangos, L. Mercadier, G. Mercurio, P. S. Miedema, K. Ollefs, B. Pfau, B. Rösner, K. Rossnagel, N. Rothenbach, A. Scherz, J. Schlappa, M. Scholz, J. O. Schunck, K. Setoodehnia, C. Stamm, S. Techert, S. M. Vinko, H. Wende, A. A. Yaroslavtsev, Z. Yin, M. Beye, Electron population dynamics in resonant non-linear x-ray absorption in nickel at a free-electron laser. *Struct. Dyn.* **10**, 054501 (2023).